J. Fluid Mech. (2025), *vol.* 1010, A29, doi:10.1017/jfm.2025.338

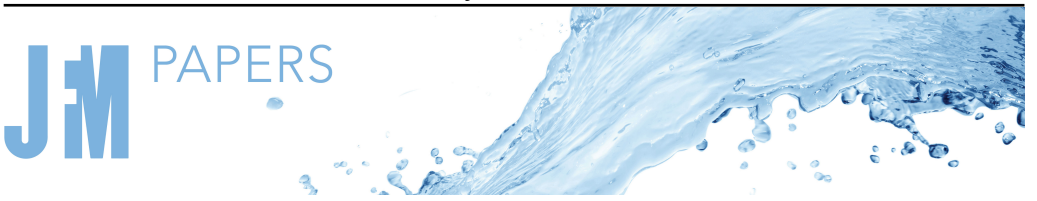

Opposition control applied to turbulent wing sections

Yuning Wang[1], **Marco Atzori**[2] **and Ricardo Vinuesa**[1]

[1]FLOW, Engineering Mechanics, KTH Royal institute of Technology, Stockholm 100 44, Sweden

[2]Department of Aerospace Science and Technologies (DAER), Politecnico di Milano, Via La Masa 34, Milan 20156, Italy

Corresponding author: Ricardo Vinuesa, rvinuesa@mech.kth.se

(Received 26 August 2024; revised 20 March 2025; accepted 23 March 2025)

Opposition control (OC) is a reactive flow-control approach that mitigates the near-wall fluctuations by imposing blowing and suction at the wall, being opposite to the off-wall observations. We carried out high-resolution large-eddy simulations to investigate the effects of OC on turbulent boundary layers (TBLs) over a wing at a chord-based Reynolds number (Re_c) of 200 000. Two cases were considered: flow over the suction sides of the NACA0012 wing section at an angle of attack of 0°, and the NACA4412 wing section at an angle of attack of 5°. These cases represent TBLs subjected to mild and strong non-uniform adverse pressure gradients (APGs), respectively. First, we assessed the control effects on the streamwise development of TBLs and the achieved drag reduction. Our findings indicate that the performance of OC in terms of friction-drag reduction significantly diminishes as the APG intensifies. Analysis of turbulence statistics subsequently reveals that this is directly linked to the intensified wall-normal convection caused by the strong APG: it energizes the control intensity to overload the limitation that guarantees drag reduction. The formation of the so-called virtual wall that reflects the mitigation of wall-normal momentum transport is also implicitly affected by the pressure gradient. Control and pressure-gradient effects are clearly apparent in the anisotropy invariant maps, which also highlight the relevance of the virtual wall. Finally, spectral analyses indicate that the wall-normal transport of small-scale structures to the outer region due to the APG has a detrimental impact on the performance of OC. Uniform blowing and body-force damping were also examined to understand the differences between the various control schemes. Despite the distinct performance of friction-drag reduction, the effects of uniform blowing are akin to those induced by a stronger APG, while the effects of body-force damping exhibit similarities to those of OC in terms of the streamwise development of the TBL although there are differences in the

turbulent statistics. To authors' best knowledge, the present study stands as the first in-depth analysis of the effects of OC applied to TBL subjected to non-uniform APGs with complex geometries.

Key words: turbulence control, turbulent boundary layers

1. Introduction

Turbulent-flow control on aircraft wings for drag reduction is of significant importance in aviation as it enhances the aerodynamic performance of aircraft, contributing to emission control and yielding substantial economic and environmental benefits (Fukagata *et al.* 2024; Wang *et al.* 2024). The primary source of drag is viscous drag (Anderson 1991), which results from the interactions of the turbulent boundary layer (TBL) on the wing surface, accounting for approximately 50 % of the total drag (Abbas *et al.* 2017). Therefore, controlling viscous drag is crucial for reducing fuel consumption in commercial aircraft. Additionally, TBLs over airfoil surfaces often experience adverse pressure gradients (APGs) or favourable pressure gradients, adding complexity to the turbulent flow. This underscores the challenge and the urgent need for effective drag-reduction strategies on wings.

Over the past decades, numerous turbulent-flow control methods have been proposed. These methods can be categorized as passive or active control, depending on whether they require an additional energy source (Gad-el Hak 1996). Passive methods, such as using riblets, modify wing configurations without additional energy to reduce skin-friction drag (Viswanath 2002). Active flow control (AFC), on the other hand, manipulates the flow field using additional energy (Vinuesa *et al.* 2022).

Active flow control can be performed in a predetermined open-loop manner where the control input is independent of the flow state (Brunton & Noack 2015). One of the celebrated open-loop methods is uniform blowing/suction, which was firstly proved by Hwang (1997). High-fidelity numerical simulations conducted by Vinuesa & Schlatter (2017) and subsequent studies (Atzori *et al.* 2020, 2021) have extensively investigated turbulent flow around a NACA4412 wing section at Reynolds numbers up to 400 000, exploring various combinations of blowing and suction. These studies reported a maximum reduction of 8 % in friction drag and 5 % in total drag (Atzori *et al.* 2020). They concluded that uniform blowing reduces skin-friction drag while increasing turbulent fluctuations, whereas uniform suction has the opposite effect. This has been confirmed experimentally (Eto *et al.* 2019) and in other numerical studies on zero-pressure-gradient (ZPG) TBLs (Fukagata *et al.* 2009; Stroh *et al.* 2012). Additionally, Albers *et al.* (2019) carried out large-eddy simulations (LESs) for assessing the effect of transversal surface waves on an airfoil at $Re_c = 400\,000$, where a drag reduction of 7.5 % was achieved.

In contrast, AFC can also be reactive, implemented in a closed-loop manner, where the control action is based on real-time flow-state sensing (as in for example Collis *et al.* (2004)). Here, machine-learning methods have been used for control and sensing (Yousif *et al.* 2023), leading to very promising results. Reactive schemes generally exhibit higher efficiency than open-loop methods (Stroh *et al.* 2015), as demonstrated in experimental studies (King 2007, 2010). One idealized reactive approach is opposition control (OC) (Choi *et al.* 1994), which reduces friction drag by using blowing and suction to suppress streamwise vortices, interrupting the self-sustaining processes near the wall, such as sweep and ejection events (Kravchenko *et al.* 1993; Orlandi & Jiménez 1994). The imposed wall

velocity, as the control name indicates, opposes the detected velocity fluctuations at a prescribed sensing plane y_s, and it is set up to ensure a zero-net-mass-flux condition at the wall.

Opposition control was first proposed by Choi *et al.* (1994) through direct numerical simulations (DNS) of fully developed turbulent channel flow (TCF) at $Re_c \approx 3300$ based on the centreline velocity U_c and channel half-width δ. In that work, various implementations of OC, including v-control, w-control and combined-control methods, were explored. The same strategies were subsequently revisited by Wang *et al.* (2016). Further studies identified the optimal locations for sensing planes and control amplitude adjustments to achieve higher drag reduction (Hammond *et al.* 1998; Chung & Talha 2011), where the control mechanism is outlined as the formulation of the so-called virtual wall (Hammond *et al.* 1998). Additionally, Ge *et al.* (2016) investigated the effect of OC on redistributing energy across the terms of the turbulent kinetic energy budget. Interestingly, a recent study has also utilized deep learning for blowing-only OC, demonstrating the potential for advanced control schemes (Li *et al.* 2021). Moreover, numerical investigations by Stroh *et al.* (2012) focus on the limitations in the practical implementation of OC. Spatially developing TBLs under OC exhibit different responses compared with TCF due to stronger fluctuations in spanwise and wall-normal velocities, as well as pressure (Jiménez *et al.* 2010). Numerical studies using LES have shown significant drag reduction and the formation of a virtual wall (Pamiés *et al.* 2007). Systematic comparisons between TBL and TCF under OC have highlighted the importance of control-region determination and the challenges posed by stronger near-wall fluctuations in TBLs (Stroh *et al.* 2015; Xia *et al.* 2015). Practical implementations, such as wall deformation combined with OC, have also been proposed and investigated (Pamiés *et al.* 2011; Dacome *et al.* 2024).

Despite these advances, most studies on TBL under OC have focused on ZPG conditions, which do not reflect the realistic scenarios on aircraft wings where non-uniform pressure gradients and finite aerodynamic bodies are involved. This fact motivates the present study, which aims to explore the interaction between OC and non-uniform APG by analysing the properties of developing TBLs over the suction sides of airfoils with different geometries at moderate Reynolds numbers. High-resolution LES was performed on a NACA0012 wing section at an angle of attack (AoA) of 0° and a NACA4412 wing section at $AoA = 5°$, both at Reynolds number of $Re_c = 200\,000$ ($Re_c = U_\infty c/\nu$, where c is the chord length and ν is the kinematic viscosity), representing mild and strong APG intensities, respectively (Tanarro *et al.* 2020). The selection of the considered wing sections was based on the availability of well-documented databases at a higher Reynolds number of $Re_c = 400\,000$ from Tanarro *et al.* (2020), which offered detailed numerical set-ups and analyses, facilitating simulation efficiency while providing robust references for validation. Note that the uncontrolled TBLs around the NACA4412 wing section up to a higher $Re_c = 1\,000\,000$ are well documented in Vinuesa *et al.* (2018). In the present study, we compare OC and uniform blowing as examples of predetermined and reactive AFC schemes for drag reduction, and include body-force damping results on the suction side of a NACA4412 (Atzori *et al.* 2021) to enhance the understanding of reactive control mechanisms applied to TBLs subjected to non-uniform APGs. To the best of the authors' knowledge, this paper represents the first numerical study documenting the application of OC to this type of flow.

The paper is organized as follows. In § 2, we introduce the numerical set-up and the implementation of control schemes. In § 3, we assess the control effects on streamwise development of the boundary layer as well as the achieved drag reduction in terms of skin-friction drag and total drag. Then in § 4, we present the results of the wall-normal profiles of turbulence statistics including mean velocity and fluctuations as well as the anisotropy

invariant maps (AIMs). In § 5, we demonstrate the results of one- and two-dimensional spectral analysis. Finally, in § 6 the conclusions of this work are presented.

2. Methodology

2.1. *High-resolution LES*

The numerical investigation of control schemes is performed using high-resolution LES of TBL on the wing section NACA0012 at 0° angle of attack and the wing section NACA4412 with AoA of 5°, both at a Reynolds number of $Re_c = 200\,000$. As described below, the present high-resolution LES employs a grid very close to that of a DNS.

All simulations are carried out with the incompressible Navier–Stokes solver Nek5000 (Fischer *et al.* 2008), which is based on the spectral-element method. The spectral-element method ensures the accuracy of the solution while maintaining computational efficiency (De Moura *et al.* 2024). Specifically, the computational domain is discretized into hexahedral elements where velocity and pressure are represented by Lagrange interpolants. Following the $\mathbb{P}_N\mathbb{P}_{N-2}$ formulation (Maday & Patera 1989), if the polynomial order is $N-1$, the velocity is defined on N^3 points per element distributed according to the Gauss–Lobatto–Legendre quadrature rule, while the pressure is defined on a staggered grid of $(N-2)^3$ points with the Gauss–Legendre distribution. For time advancement in the incompressible Navier–Stokes equations, the nonlinear terms are solved by explicit third-order extrapolation (EXT3), whereas the viscous terms are solved using an implicit third-order backward scheme (BDF3). To address aliasing errors, overintegration is implemented by oversampling the nonlinear terms by a factor of 3/2 of the adopted polynomial order in each direction. This simulation framework has been previously used for high-fidelity simulations of complex turbulent flows, see for example the work by Noorani *et al.* (2016).

The high-resolution LES captures the effects of the smallest turbulent scales via a subgrid-scale model based on a time-independent relaxation-term filter developed by Negi *et al.* (2018). The filtering operation is performed implicitly through a volume force accounting for the dissipation of unresolved turbulent scales, and this operation is conducted ensuring that continuity is preserved. Including the LES filter, the governing equations of the system are the incompressible continuity and momentum equations in non-dimensional form, expressed as

$$\frac{\partial u_i}{\partial x_i} = 0, \tag{2.1}$$

$$\frac{\partial u_i}{\partial t} + u_j \frac{\partial u_i}{\partial x_j} = -\frac{\partial p}{\partial x_i} + \frac{1}{Re_c}\frac{\partial^2 u_i}{\partial x_i x_j} - \mathcal{H}(u_i), \tag{2.2}$$

where the usual index notation is used, u_i denotes the velocity components in Cartesian coordinates, p denotes the pressure and $\mathcal{H}$ is the high-pass filter ensuring that the LES is acting on a subset of modes within each spectral element. The implementation of this filter in Nek5000 has been validated by Vinuesa *et al.* (2018).

The computational domain is a C-mesh extending $6c$ horizontally and $4c$ vertically. The leading and trailing edges of the airfoil are located $2c$ and $3c$ from the front boundary of the domain, respectively. The spanwise width of the domain for simulating the NACA4412 wing section is $0.2c$ and for the NACA0012 wing section is $0.1c$. This set-up has been validated in previous works (Vinuesa *et al.* 2018; Tanarro *et al.* 2020; Atzori *et al.* 2021), confirming that the spanwise widths are sufficient to capture the range of active scales as well as the largest turbulent structures in the TBL over the airfoil. The computational

domain for the NACA4412 and NACA0012 consists of 127 000 and 220 000 spectral elements, respectively.

The desired near-wall spatial resolution of the current simulation is expressed in terms of viscous units such that $\Delta x_t^+ < 18.0$, $\Delta y_n^+ < (0.64, 11.0)$ and $\Delta z^+ < 9.0$ in the wall-tangential, wall-normal and spanwise directions, respectively. To achieve this resolution, polynomial orders of $P = 11$ and $P = 7$ are adopted for simulating the flow around the NACA4412 and NACA0012 cases, respectively. This leads to total number of grid points of $\approx 1.1 \times 10^8$ and $\approx 2.2 \times 10^8$ for NACA0012 and NACA412 cases, respectively. Note that the viscous length $l^* = \nu/u_\tau$ is defined in terms of the friction velocity $u_\tau = \sqrt{\tau_w/\rho}$ (where $\tau_w = \rho\nu(\,\mathrm{d}U_t/\,\mathrm{d}y_n)_{y_n=0}$ is the mean wall-shear stress and ρ is the density) and fluid kinematic viscosity ν. The spatial resolution in the wake follows $\Delta_x/\eta < 9$, where $\eta = (\nu^3/\epsilon)^{1/4}$ represents the Kolmogorov scale. Note that ϵ is the local isotropic dissipation. The proposed mesh has been validated for the present subgrid-scale approach by Negi *et al.* (2018), demonstrating a very good agreement between DNS and LES results for a simulation of a NACA4412 airfoil at $Re_c = 400\,000$.

Dirichlet boundary conditions were adopted for the front, upper and lower boundaries, imposing an estimated far-field velocity distribution obtained via a supporting Reynolds-averaged Navier–Stokes (RANS) simulation. The k–ω shear-stress transport model (Menter 1994) was employed for the RANS simulation, where a circular domain with a radius of $200c$ is considered. For the outlet, the boundary condition developed by Dong *et al.* (2014) is used, preventing the uncontrolled influx of kinetic energy through the outflow boundaries. This boundary condition, which is a modified Neumann boundary condition, has been developed and extensively tested to assure the stability of numerical simulations with a severely truncated computational domain, where negative velocities from the outlet boundary are prevented. The boundary layer is tripped at $x/c = 0.1$ from the leading edge on both suction and pressure sides of the wing section, following the approach proposed by Schlatter & Örlü (2012). The tripping consists of a wall-normal localized body force, producing strong, time-dependent streaks which eventually break down leading to a transition process (Vinuesa *et al.* 2017), with effects similar to those of experimental devices (Schlatter & Örlü 2012).

The simulation procedure is as follows. (i) Use the solution of the RANS simulation as the initial condition for velocity and pressure fields. (ii) Run the simulation at a polynomial order of $P = 5$ for six flow-over times, and then for 10 flow-over times at a polynomial order of $P = 7$. (iii) Run the simulation at the target polynomial order of $P = 11$ for 11 time units while accumulating samples to compute the statistics. This process ensures a smooth increase of resolution from the initial condition, as well as the identification and removal of initial transients (Vinuesa *et al.* 2017). Note that one flow-over time is defined as the time required for a fluid particle moving with the incoming velocity U_∞ to travel a distance of c. For simulating uncontrolled NACA0012 cases, we also use the solution of the RANS simulation as the initial condition, and directly start running the simulation at a polynomial order of $P = 7$ for seven flow-over times, and subsequently run for 20 flow-over times for sampling the statistics. Running for 20 flow-over times is necessary due to fact that the spanwise width of the NACA0012 wing section is half of that of the NACA4412 in the present study, see Vinuesa *et al.* (2016*b*, 2018) for additional details. For the cases with the control scheme applied, we start the simulation from the fully developed turbulent field of the uncontrolled case. Each controlled case on the airfoil NACA4412 and NACA0012 requires approximately 10 and 20 flow-over times, respectively, to obtain converged statistics. The computational cost to simulate 10 flow-over times is approximately 1×10^6 CPU hours on a Cray-XC 40 system.

Case notation	Airfoil	AoA	Control over suction side ($0.25 < x/c < 0.86$)	Colour code
Ref1	NACA0012	0°	Uncontrolled	
BL1			Uniform blowing with 0.1 $\%U_\infty$	
OC1			Opposition control with $y_s^+ = 15$	
Ref2	NACA4412	5°	Uncontrolled	
BL2			Uniform blowing with 0.1 $\%U_\infty$	
OC2			Opposition control with $y_s^+ = 15$	
BD2			Body-force damping with $y_n^+ < 20$	

Table 1. Control configurations considered in the present study at $Re_c = 200\,000$. The coloured squares denote the colour code for each case.

2.2. *Control schemes and configurations*

In the present study, we investigate five different control cases, whose configurations are summarized in table 1. In cases OC1 and BL1, OC and uniform blowing are applied on the suction side of the NACA0012 airfoil between the streamwise locations of $x/c = 0.25$ and 0.86, following the set-up by Vinuesa & Schlatter (2017). Cases OC2 and BL2 involve OC and uniform blowing applied to the suction side of the NACA4412 airfoil within the same streamwise range. Additionally, we include a case BD2 from the work of Atzori *et al.* (2021), which applies body-force damping to the suction side of the NACA4412 airfoil within the same streamwise range.

Opposition control is implemented as a Dirichlet boundary condition that imposes a velocity at the wall opposite to the detected wall-normal velocity at a prescribed sensing plane y_s, thereby attenuating sweep and ejection events near the wall (Choi *et al.* 1994). A schematic of the OC mechanism is shown in figure 1(*a*). This control method, also known as v-control as defined by Choi *et al.* (1994), involves the control input at the wall given by

$$v(x, 0, z, t) = -\alpha \left[v(x, y_s, z, t) - \langle v(x, y_s, t) \rangle \right], \tag{2.3}$$

where α is a positive amplification factor set to unity in the present study. Note that the spatial mean $\langle v(x, y_s, t) \rangle$ is subtracted to maintain a zero-net-mass-flux condition at the wall. Due to inherent streamwise non-homogeneity, the spatial mean is obtained by averaging the instantaneous wall-normal velocity component in the spanwise direction.

The sensing plane y_s is set to $y_s^+ = 15$ based on previous studies (Hammond *et al.* 1998), which showed that the maximum drag reduction rate was achieved at this position in viscous units. The wall-normal location in outer units is calculated as $y_s = \nu y_s^+ / u_\tau$, where u_τ is the friction velocity of the uncontrolled case. As the local friction velocity u_τ varies with x, y_s is non-uniform to maintain the same dimensionless distance from the wall, as shown in figure 1(*b*).

We performed a series of tests on the sensing plane location from $y_s^+ = 7.5$ to 17.5, showing that positions below 12.5 and above 15.0 increase skin-friction drag, while finer calibrations between $12.5 \leq y_s^+ \leq 15.0$ yield little improvement. We also explored applying OC on both the suction and pressure sides of NACA4412 but found negligible improvement for drag reduction. Thus, we focus on applying control over the suction side in the present study.

To validate our code implementation, we applied OC to TCF at $Re_\tau = 180$ and $y_s^+ = 15$ using DNS in the same solver. In TCF, OC is applied on both walls, with the spatial average in (2.3) computed in the streamwise and spanwise directions due to homogeneity and

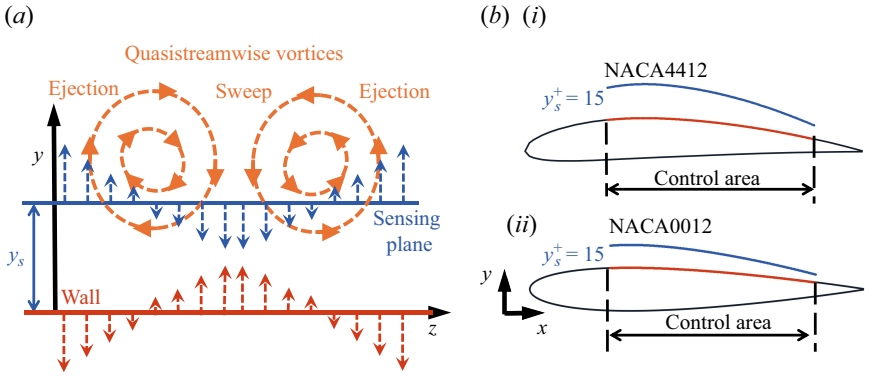

Figure 1. (*a*) Schematic view of the OC scheme, adapted from Stroh *et al.* (2015). (*b*) Schematic of control configurations for (i) NACA4412 and (ii) NACA0012.

periodicity (Stroh *et al.* 2015). This leads to zero for the spatial average as expected in TCF. The computational domain had the following dimensions: $\Omega = L_x \times L_y \times L_z = 10h \times 2h \times 5h$ (where h is the channel half-height), with $N_x \times N_y \times N_z = 270 \times 144 \times 270$ grid points and a polynomial order of 11, at a Reynolds number based on bulk velocity U_b of $Re_b = 2\,800$. Turbulence statistics were computed for about 600 eddy turnover times after the controlled flow was fully developed. Our results, showing a drag reduction rate of 22.46 %, agree closely with the 22.96 % reported by Choi *et al.* (1994), who used a similar numerical set-up with same control configuration, thus validating our OC implementation.

Uniform blowing is implemented as a boundary condition of Dirichlet type at the wall, imposing the horizontal and vertical velocity components such that the magnitude of the wall-normal velocity equals the desired control intensity. A constant intensity of $0.1\,\%U_\infty$ was adopted. Body-force damping imposes a volume force defined as $g(v_n) = -\gamma(v_{n,x}, v_{n,y}, 0)$ within the wall-normal region $y_n^+ < 20$, where $v_{n,x}$ and $v_{n,y}$ are the projections of the wall-normal component of the instantaneous velocity in the horizontal and vertical directions, respectively, and γ is the coefficient of the body-force intensity (Stroh *et al.* 2016). The momentum equation incorporating this volume force is expressed as

$$\frac{\partial u_i}{\partial t} + u_j \frac{\partial u_i}{\partial x_j} = -\frac{\partial p}{\partial x_i} + \frac{1}{Re_c}\frac{\partial^2 u_i}{\partial x_i x_j} - \mathcal{H}(u_i) + g(v_n). \tag{2.4}$$

Note that the γ value is calibrated to $\gamma = 32.5$ to achieve a skin-friction reduction comparable to that of uniform blowing with an intensity of $0.1\,\%U_\infty$ between $x/c \approx 0.45$ and 0.8. This control scheme is included to allow a comparison between different closed-loop control strategies. The implementation of uniform blowing and body-force damping is the same that has been already employed by Atzori *et al.* (2020, 2021).

3. Control effects on integral quantities

In this section, we first assess the streamwise development of the TBL in terms of integral quantities. Subsequently, based on the assessments, we evaluate the control efficiency for drag reduction.

3.1. *Streamwise development of the boundary layer*

The non-uniform APGs in the various cases lead to different interactions with the control schemes. We consider four parameters, namely the Clauser pressure-gradient parameter

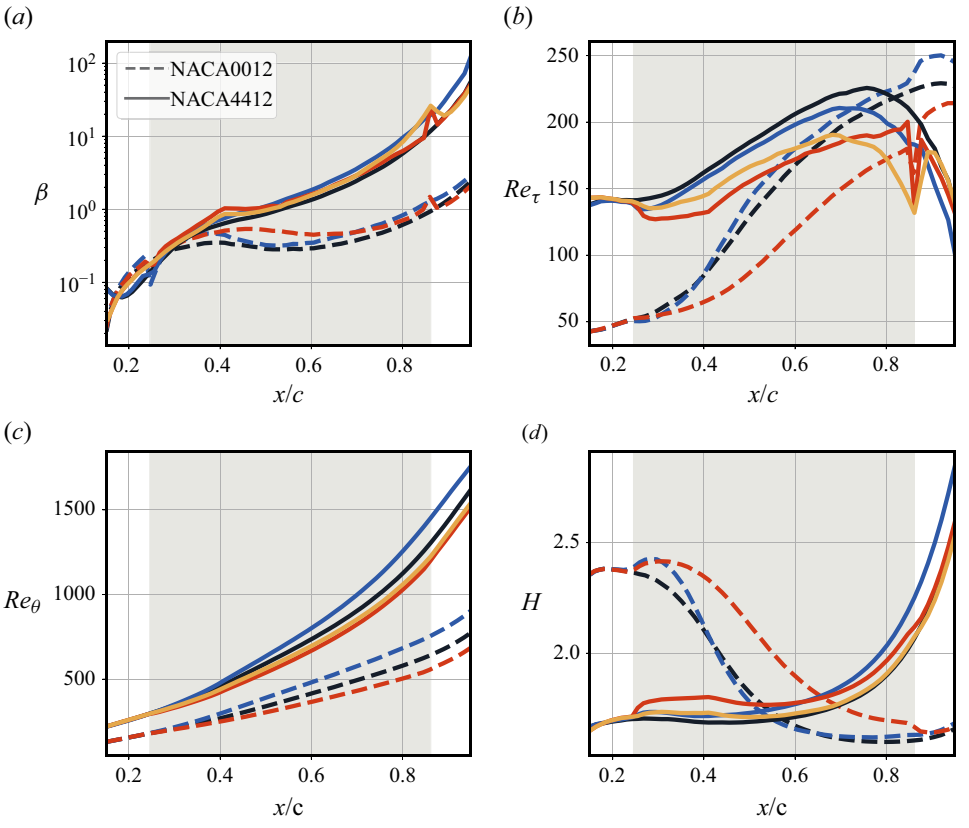

Figure 2. (*a*) Clauser pressure-gradient parameter (β), (*b*) friction Reynolds number (Re_τ), (*c*) Momentum-thickness-based Reynolds number (Re_θ) and (d) shape factor H distributions on suction side of NACA0012 (dashed lines) and NACA4412 (solid lines). Note that the control region is indicated in grey. The colour code follows table 1.

$\beta = \delta^*/\tau_w \, \mathrm{d}P_e/\,\mathrm{d}x_t$ (where δ^* is the displacement thickness and P_e is the pressure at the boundary-layer edge), the friction Reynolds number $Re_\tau = \delta_{99} u_\tau/\nu$, the momentum-thickness-based Reynolds number $Re_\theta = U_e\theta/\nu$ and the shape factor $H = \delta^*/\theta$. The streamwise evolutions are depicted in figure 2, and table 2 reports the parameters obtained at $x/c = 0.4$ and 0.75. Note that δ_{99} and U_e are the 99 % boundary-layer thickness and the mean velocity at the boundary-layer edge, which are both obtained by the method proposed by Vinuesa *et al.* (2016*a*).

Figure 2(*a*) shows the streamwise evolution of the Clauser pressure-gradient parameter along the suction sides of the wing sections. It can be observed that the β curve of case Ref2 is more prominent with respect to Ref1 and exhibits a rapid increase, which is attributed to the presence of the camber and higher angle of attack (Tanarro *et al.* 2020). Control schemes generally increase β within the control region. Opposition control and body-force damping significantly reduce τ_w, enhancing β, whereas uniform blowing, though less effective in reducing τ_w, increases δ^* more notably. It can be observed that uniform blowing extends the increment beyond the control region, while the reactive schemes recover β to the uncontrolled states outside the control region. Note that the profiles of OC and body-force damping exhibit a peak at the edge of the control area, reflecting strong wall-pressure fluctuations triggered by the control activations (Stroh *et al.* 2015).

Case	x/c	u_τ	θ	δ^*	δ_{99}	β	Re_τ	Re_θ	H
Ref1	0.40	0.0459	0.0012	0.0025	0.0097	0.35	88	275	2.1
BL1	–	0.0439	0.0014	0.0028	0.0104	0.45	91	305	2.1
OC1	–	0.0376	0.0011	0.0026	0.0088	0.51	66	254	2.3
Ref2	0.40	0.0635	0.0018	0.0029	0.0130	0.64	164	470	1.7
BL2	–	0.0599	0.0018	0.0031	0.0133	0.76	159	494	1.7
OC2	–	0.0522	0.0016	0.0029	0.0127	1.03	132	435	1.8
BD2	–s	0.0571	0.0017	0.0029	0.0128	0.86	146	452	1.7
Ref1	0.75	0.0507	0.0025	0.0041	0.0202	0.45	205	527	1.6
BL1	–	0.0470	0.0030	0.0048	0.0226	0.60	213	617	1.6
OC1	–	0.0447	0.0022	0.0038	0.0179	0.58	160	459	1.7
Ref2	0.75	0.0417	0.0043	0.0078	0.0270	3.40	225	988	1.8
BL2	–	0.0358	0.0048	0.0092	0.0294	5.18	210	1096	1.9
OC2	–	0.0376	0.0040	0.0074	0.0252	3.93	189	902	1.8
BD2	–	0.0356	0.0041	0.0074	0.0259	4.43	184	931	1.8

Table 2. Integral quantities at $x/c = 0.4$ and 0.75.

Figure 2(*b*) illustrates the distribution of Re_τ along the suction side, with case Ref1 showing continuous growth, and case Ref2 saturating before declining under the influence of increasingly intense pressure gradient. Opposition control significantly reduces Re_τ by effectively lowering u_τ, which is mirrored by body-force damping. In contrast, uniform blowing, by increasing δ^*, leads to less reductions in Re_τ, and may even increase it as observed in case BL1.

The evolution of Re_θ, as shown in figure 2(*c*), is notably affected by the APG, which decelerates the flow and increases the momentum thickness θ. Both OC and body-force damping counteract these effects, whereas uniform blowing exacerbates them. The contrasting impacts of these control strategies are significant, as the momentum thickness is closely related to skin friction at the wall. Note that the concept of virtual origin outlined by Stroh *et al.* (2016) to describe the downstream control effect is difficult to evaluate for APG TBL due to the complex implication of flow history.

Finally, the evolution of the shape factor H is depicted in figure 2(*d*). It can be observed that case Ref2 shows a remarkable increase throughout, while case Ref1 reaches a plateau and then decreases, suggesting a shift towards a more turbulent state. A higher H is indicative of a laminar-like state (or a flow with decreased near-wall fluctuations as in large APGs), with values around 2.6 typical for Blasius boundary layers, whereas turbulent states in ZPG TBL usually range from 1.2–1.6 (Schlatter & Örlü 2010).

3.2. *Control efficiency*

Based on the assessment of streamwise development, in this section, we first describe how control schemes affect skin friction, and then demonstrate the achieved aerodynamic efficiencies as they are applied.

To evaluate the modification of friction drag we examine the skin-friction coefficient c_f, which is defined as $c_f = \tau_w/(1/2\rho U_e^2)$.

The drag-reduction rate $R(x)$, according to the metrics proposed by Kametani *et al.* (2015), is defined as

$$R(x) = 1 - \frac{c_f(x)}{c_f^{ref}(x)}, \tag{3.1}$$

where superscript ref denotes the uncontrolled case. In addition to the drag reduction, the net-energy saving $E(x)$ is evaluated as

$$E(x) = 1 - \frac{\left(c_f(x) + \psi_{in}(x)\right)}{c_f^{ref}(x)}, \tag{3.2}$$

where $\psi_{in}(x)$ is the input power calculated as $\psi_{in}(x) = 1/2||v_{wall}||^3$ according to the approach of Kametani *et al.* (2015). In the present study, the input power for OC is $\psi_{in} \sim O(10^{-6})$ while in the case of uniform blowing it is $\psi_{in} \sim O(10^{-12})$. The skin-friction coefficient is around $O(10^{-3})$, suggesting that $R \approx E$ as discussed by Kametani *et al.* (2015). Another approach for evaluating energy gain (G) is proposed by Bewley *et al.* (2001), considering the impact of the wall pressure fluctuation p'_w on the input power, which is expressed as

$$G(x) = \frac{P_S}{P_I}, \tag{3.3}$$

where the input power is $P_I = \langle |p'_w v_w| \rangle + \rho \langle |v_w^3| \rangle$ and the power saving is defined as $P_S = U_\infty(\tau_{w,ref} - \tau_w)$. Note that $P_I \sim O(10^{-6})$ and $\sim O(10^{-5})$ for the control schemes applied on the NACA0012 and NACA4412, respectively.

None of these cost estimates are not meaningful for body-force damping, which acts as a volume force, but it should be noted that even for OC and uniform blowing they only provide a lower estimate of the actuation cost. A more realistic estimate requires introducing hypotheses on the actuators (see for example Fahland *et al.* (2023)), and it is considered beyond the scope of the present numerical work.

Figure 3(*a*) illustrates the streamwise development of c_f along the suction side of the wing sections. The variation in c_f closely follows the evolution of the Clauser pressure-gradient parameter β, leading to different control performances, as shown in figure 3(*b*). Opposition control achieves a peak of $R = 40\,\%$ at $x/c \approx 0.5$ for case OC1 and approximately 30 % at $x/c = 0.4$ for case OC2. Downstream of the saturation point, OC1 maintains a plateau at $R \approx 20\,\%$, whereas OC2 continues to decline. A similar plateau was observed when applying OC on ZPG TBLs within the control region (Pamiés *et al.* 2007; Stroh *et al.* 2015). The decreasing R in OC2 is linked to stronger APG conditions. Note that the peaks at the edge of control region correspond to Re_τ profiles, influenced by strong pressure fluctuations due to boundary condition changes. The other reactive control scheme, BD2, peaks at approximately 20 % at $x/c = 0.4$, with a steady increase in regions dominated by strong APG, attributed to the calibrated amplitude γ. Additionally, BD2 exhibits a peak at the edge of control region, being similar to OC2. The performance of uniform blowing varies with the wing case; BL2 shows a continuous increase from $R \approx 10\,\%$ up to 40 %, indicating a nearly constant absolute reduction in c_f (Kametani *et al.* 2015; Stroh *et al.* 2016). In contrast, BL1 reaches saturation at $R \approx 20\,\%$ at $x/c = 0.3$, before decreasing to a minimum of $\approx 2\,\%$ at $x/c \approx 0.5$.

Figure 3(*c*) depicts the energy gain G expressed in logarithmic scale along the suction side of the wings. It is observed that the control schemes overall achieve less energy gain on the suction side of the NACA4412 than that of the NACA0012 case by approximately an

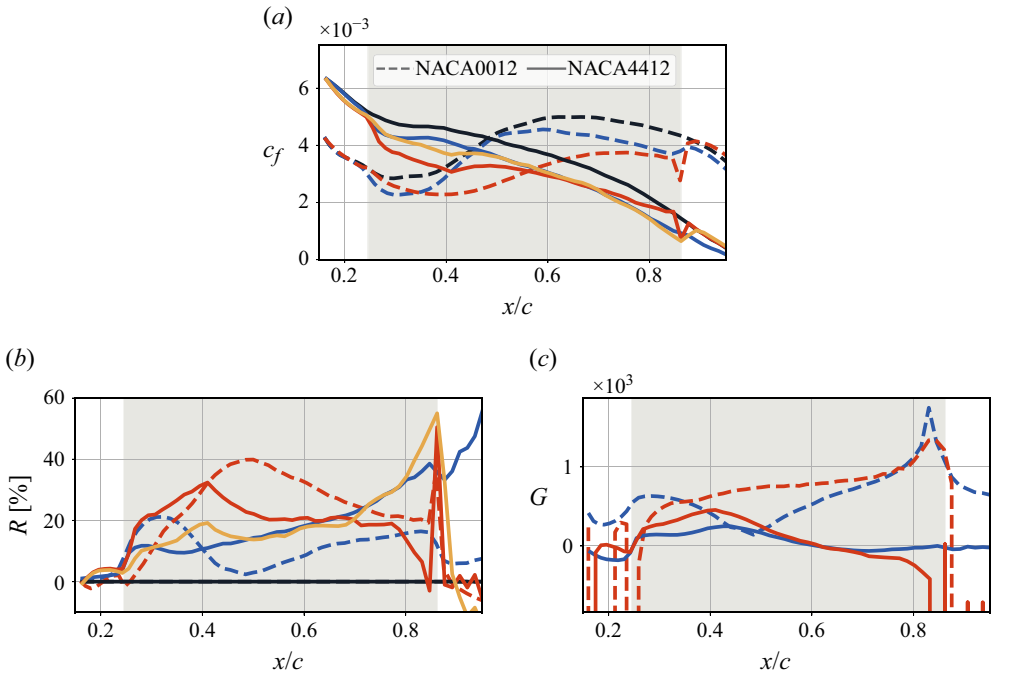

Figure 3. (*a*) Skin-friction coefficient (c_f), (*b*) spatial development of drag-reduction rate(R) and (*c*) energy gain (G) over the suction side of NACA0012 (dashed lines) and NACA4412 (solid lines). Note that the control region is coloured in grey. The colour code follows table 1.

order of magnitude. This is linked to the magnitude of the wall-pressure fluctuation. The spatial evolutions of G exhibits similarity with that of the R, where the G trends achieved by control schemes increase and descend with downstream development over the suction side of the NACA4412 and NACA0012, respectively. Additionally, over the pressure side, none of the considered control schemes impact c_f.

Next, we evaluate the control effects on the aerodynamic efficiency (i.e. lift-to-drag ratio) of the airfoil, which is typically expressed as the ratio between lift and drag coefficients. The lift and drag coefficients are defined as $C_l = f_l/(bq)$ and $C_d = f_d/(bq)$, respectively, where we denote b as spanwise width, whereas f_l/b as the lift force per unit length, f_d/b as the drag force per unit length and q as the free stream dynamic pressure ($q = 1/2\rho U_\infty^2$). Note that the f_l/b and f_d/b are calculated by integrating wall-shear stress and the pressure force around the wing section and projecting them on the directions parallel and perpendicular to the incoming flow, respectively. To investigate the contributions of the drag coefficient C_d, we further decompose it into skin-friction drag $C_{d,f} = f_{d,f}/(bq)$ and pressure drag $C_{d,p} = f_{d,p}/(bq)$.

Table 3 summarizes the values of the integrated lift (C_l), integrated skin-friction ($C_{d,f}$), and pressure ($C_{d,p}$) contributions to the total drag (C_d) and the aerodynamic efficiency ($L/D = C_l/C_d$) for the cases considered in the present study. Note that as the C_l for case Ref1 is approximately 0 and thus $L/D \approx 0$, whereas the OC1 and BL1 increase and decrease the C_l by a magnitude of $O(10^{-3})$, respectively, which is a minor change. We therefore focus on the modification of C_d for those cases. Uniform blowing applied on the suction side reduces the friction drag force thus reduces the $C_{d,f}$ while increasing the $C_{d,p}$, which is also reported by Atzori *et al.* (2020). Consequently, case BL1 does not change the C_d and case BL2 increase the C_d by 2.8 % with respect to the uncontrolled

Case	C_l	$C_{d,f}$	$C_{d,p}$	$C_d = C_{d,f} + C_{d,p}$	L/D
Ref1	≈ 0	0.0105	0.0014	0.0118	≈ 0
BL1	–	0.0101 (−3.8 %)	0.0017 (+21.4 %)	0.0118 (+0.0 %)	–
OC1	–	0.0097 (−7.6 %)	0.0014 (+0.0 %)	0.0110 (−6.8 %)	–
Ref2	0.8670	0.0128	0.0087	0.0215	41
BL2	0.8330 (−4.0 %)	0.0122 (−4.7 %)	0.0099 (+13.8 %)	0.0221 (+2.8 %)	38 (−7.3 %)
OC2	0.8734 (+1.0 %)	0.0121 (−5.5 %)	0.0083 (−4.6 %)	0.0204 (−5.1 %)	43 (+4.9 %)
BD2	0.8790 (+1.4 %)	0.0121 (−5.5 %)	0.0083 (−4.6 %)	0.0204 (−5.1 %)	43 (+4.9 %)

Table 3. Integrated lift (C_l), integrated skin-friction ($C_{d,f}$), and pressure ($C_{d,p}$) contributions to the total drag (C_d), and the aerodynamic efficiency (L/D) for the cases considered in the present study. The values in the parentheses report the relative changes obtained by control.

case. However, applying OC on the suction side (case OC1 and OC2) reduces both $C_{d,f}$ and $C_{d,p}$ simultaneously. The resulting reductions in C_d are 6.8 % and 5.1 % for case OC1 and OC2, respectively, being similar to the effects of applying body-force damping on the suction side.

4. Control effects on turbulence statistics

The APG intensifies wall-normal convection, significantly affecting the outer region of the boundary layer (Harun *et al.* 2013). This has a substantial impact on the turbulence statistics, which is crucial for understanding the different efficiencies of the various drag-reduction schemes.

In this section, we analyse the mean flow and Reynolds stress. We assess inner- and outer-scaled profiles at $x/c = 0.75$, corresponding to strong APG conditions. Note that the statistics are expressed in terms of wall-tangential (t) and normal (n) directions relative to the wing surface, using the local quantities to determine the corresponding inner and outer scales for all cases.

4.1. *Mean velocity profile*

Figure 4 depict the inner-scaled mean wall-tangential velocity profiles U_t^+ at $x/c = 0.75$ on the suction side of the wing sections, respectively. Stronger APGs are known to enhance the wake region in inner-scaled profiles (Spalart & Watmuff 1993; Monty *et al.* 2011). This effect remains evident in the uncontrolled cases at $x/c = 0.75$, where case Ref2 exhibits a higher pressure gradient ($\beta = 3.4$) than Ref1 ($\beta = 0.45$). Note that the stronger APG results in a steeper slope in the very incipient overlap region found there (Spalart & Watmuff 1993).

Opposition control causes a significant downward shift in the viscous sublayer and an increase in U_t^+ starting from $y_n^+ \approx 7$, becoming more pronounced with increasing APG intensity. Choi *et al.* (1994) related this shift with the displacement of the so-called virtual origin. However, due to the complex history effects of the APGs studied here, it remains challenging to conclusively evaluate this impact in the current study (Atzori *et al.* 2021). The prominent wake region is further intensified by the OC due to the different reduction in u_τ at the various streamwise locations.

Uniform blowing increases the inner-scaled velocity in the wake region compared with the reference. In the buffer layer, this control scheme increases U_t^+ but to a less extent than OC, being similar to the effects observed under stronger APGs (Spalart & Watmuff 1993; Harun *et al.* 2013). The influence on the viscous sublayer is less pronounced than that of

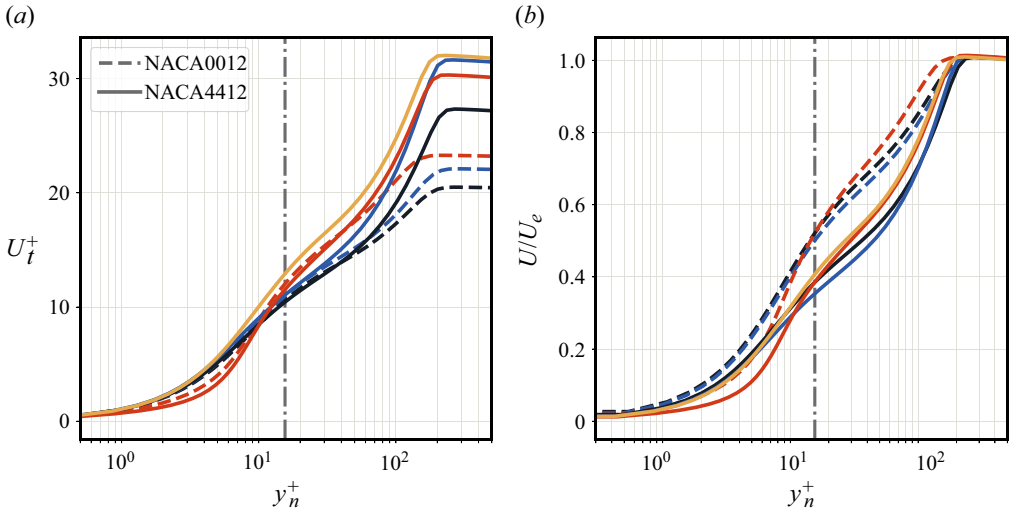

Figure 4. (*a*) Inner- and (*b*) outer-scaled mean wall-tangential velocity U_t as a function of the inner-scale wall-normal distance y_n^+ at $x/c = 0.75$ on suction side of (*a*) NACA0012 and (*b*) NACA4412. The prescribed sensing plane for OC of $y_s^+ = 15$ is indicated by a grey dash–dotted line. The colour code follows table 1.

OC but is nonetheless significant. Body-force damping impacts U_t^+ similarly to uniform blowing but exhibits additional complexity. For instance, case BD2 exhibits higher U_t^+ than BL2 across most wall-normal distances, despite achieving comparable friction-drag reduction at $x/c = 0.75$. This similarity extends to the boundary-layer edge, where it aligns closely with BL2.

Control impacts on inner-scaled profiles are largely tied to modifications in friction velocity. Therefore, we further assessed the outer-scaled profiles U_t/U_e at $x/c = 0.75$ (figure 4). The OC profiles are notably shifted downward in the viscous sublayer, with this effect extending into the buffer layer. The controlled profiles subsequently realign with the reference case around the position of the prescribed sensing plane ($y_n^+ = 15$). Beyond this wall-normal position, OC increases the outer-scaled mean velocity.

Body-force damping slightly reduces velocity in the viscous sublayer due to a decrease in friction velocity. Its effects above this layer are similar to those of OC, with case BD2 aligning closely with OC2 but showing slight variations in velocity at higher wall-normal distances. Uniform blowing, in contrast, consistently leads to lower outer-scaled profiles than the uncontrolled cases, particularly under stronger APGs. This is primarily linked to reduced friction velocity.

4.2. *Reynolds-stress components*

The intensified wall-normal convection caused by APG significantly affects momentum transfer across the entire boundary layer (Skaare & Krogstad 1994), which therefore impacts the wall-normal profiles of the Reynolds-stress-tensor components. In figure 5, we show the inner-scaled fluctuations of the wall-tangential velocity components as a function of the inner-scaled wall-normal distance at $x/c = 0.75$. The profile of case Ref2 exhibits a more pronounced inner peak compared with case Ref1, indicating that the increased APG amplifies wall-tangential fluctuations at all wall-normal distances, which is connected to the lower friction velocity under intense APG conditions. Additionally, a noticeable effect of the stronger APG is the emergence of an outer peak (Monty *et al.* 2011) due to enhanced wall-normal convection, which is more prominent.

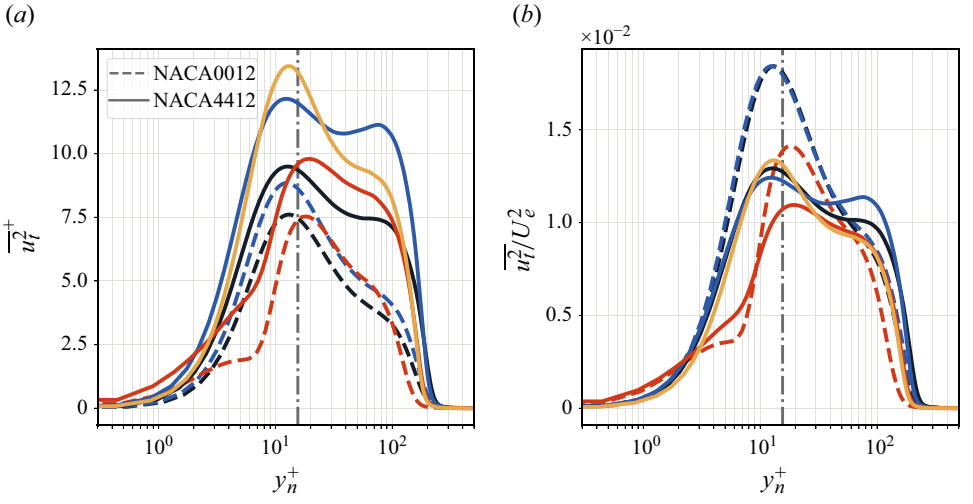

Figure 5. (*a*) Inner- and (*b*) outer-scaled fluctuations of wall-tangential velocity components $\overline{u_t^2}$ as a function of the inner-scale wall-normal distance y_n^+ at $x/c = 0.75$ on suction side of NACA0012 (dashed lines) and NACA4412 (solid lines). The prescribed sensing plane of OC ($y_s^+ = 15$) is indicated by a grey dash–dotted line. The colour code follows table 1.

For the OC cases, the inner-scaled profiles exhibit higher inner and outer peaks than the uncontrolled case, due to a reduction in friction velocity. In particular, the inner peak shifts farther from the wall while the outer peak descends towards the wall, both by approximately one wall unit. The assessment of the outer-scaled profiles reveals that OC reduces both inner and outer peaks, whereas the reduction on the inner peak is more prominent. Furthermore, OC significantly attenuates wall-tangential fluctuations in the buffer layer, especially under milder adverse-pressure gradient conditions, implying that the flow history has impact on the control performance. Note that the near-wall enhancement of $\overline{u_t^2}^+$ is due to the control input (Choi *et al.* 1994).

In contrast, uniform blowing further intensifies both the near-wall and outer peaks of $\overline{u_t^2}^+$ compared with the uncontrolled cases, which is similar to the effect of stronger APG. Moreover, the inner-scaled profile of case BD2 exhibits a higher inner peak and a lower outer peak compared with uniform blowing, while the outer-scaled profile indicates that body-force damping attenuates the outer peak but energize the inner peak, being different from the effects of OC.

Since OC is specifically designed to mitigate convective momentum transport in the wall-normal direction (Choi *et al.* 1994), it is natural to examine wall-normal velocity fluctuations. We illustrate the inner- and outer-scaled profiles at $x/c = 0.75$ in figures 6(*a*) and 6(*b*), respectively. Due to the intensified wall-normal convection caused by the stronger APG, the wall-normal velocity fluctuations intensify and the location of the peak moves farther from the wall. This position approximately aligns with the outer-peak location of $\overline{u_t^2}^+$ d (Atzori *et al.* 2021). In particular, case Ref2 exhibits a more prominent outer peak, which is independent to the scaling, being located approximately 10 wall units farther from the wall compared with case Ref1. Note that the inherent low-Reynolds-number effect in case Ref1 does not significantly impact $\overline{v_n^2}$.

For OC, the modifications of the outer peak of the inner-scaled profiles are more prominent under intense APG conditions, which is due to the variations in friction velocity

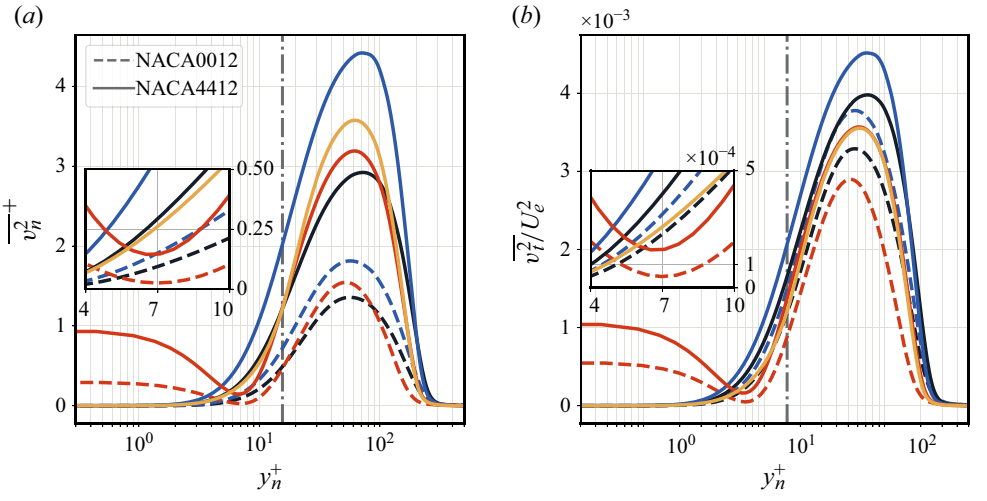

Figure 6. Inner-scaled fluctuations of wall-normal velocity components $\overline{v_n^2}$ as a function of the inner-scale wall-normal distance y_n^+ at streamwise location of $x/c = 0.4$ (*a*) and $x/c = 0.75$ (*b*) on suction side of NACA0012 (dashed lines) and NACA4412 (solid lines). The dashed lines and solid lines denote the configurations for NACA0012 and NACA4412, respectively. The prescribed sensing plane of OC ($y_s^+ = 15$) is indicated by a grey dash–dotted line. The colour code follows table 1.

by assessing the outer-scaled profiles. Note that the modified outer peak exhibits an inward shift by approximately one wall unit, coinciding with the outward shift of $\overline{u_t^2}$.

In the near-wall region, the presence of the non-zero value at the wall is due to the control input (Choi *et al.* 1994), and farther from the wall, the intensified $\overline{v_n^2}$ gradually decreases due to more intense momentum transport in the wall-normal direction. In particular, examining the inner-scaled profiles at the wall, case OC2 yields $\overline{v_{n,w}^2}^+ \approx 0.9$, which is more than triple that of case OC1 (≈ 0.3). The results indicate that the stronger APG induces higher control input due to the enhanced wall-normal convection. As outlined by Chung & Talha (2011), the maximum drag reduction is achieved around $\overline{v_{n,w}^2}^+ = 0.25$, beyond which the drag-reduction rate R decreases regardless of the prescribed sensing plane. This claim should also hold for the present study since the small-scale near-wall structures are invariant to the geometry and the flow type. We therefore examined the downstream evolutions of R and $\overline{v_{n,w}^2}^+$ in figure 7. It can be observed that R starts decreasing after the inner-scaled wall-normal fluctuations at the wall exceed 0.25. Under strong APG conditions, the wall-normal fluctuations at the wall are much higher and raise much more quickly with the downstream development. This is an indication that is the intensified wall-normal convection induced by the APG that significantly affects the control performance, resulting in the aforementioned narrow range of the effective sensing-plane position.

Furthermore, at $y_n^+ \approx 7$, the profiles of OC exhibit local minima close to zero, as illustrated in the inset of each panel in figure 6. This wall-normal distance corresponds to approximately half of the wall-normal location of the sensing plane $y_s^+ = 15$, providing clear evidence of the so-called virtual wall (Hammond *et al.* 1998). Hammond *et al.* (1998) outlined that the virtual wall results from the weakening of sweep and ejection events caused by OC, preventing convective momentum transport across the plane of the virtual wall. By prescribing the sensing plane at the same wall-normal position $y_s^+ = 15$, Hammond *et al.* (1998) reported the virtual wall in TCF at $y_v^+ \approx 7.5$, and Pamiés *et al.*

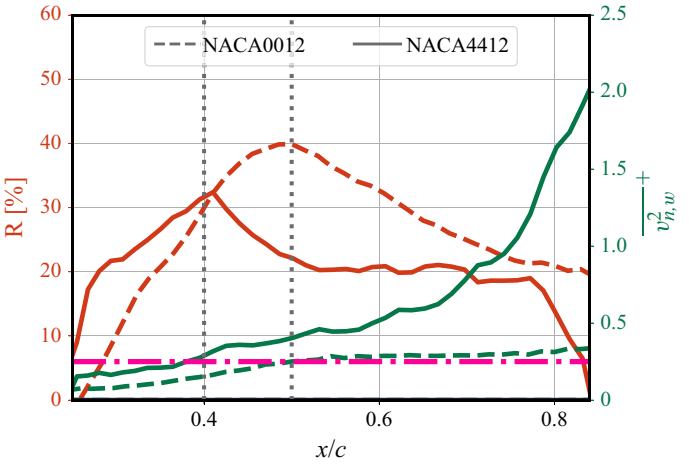

Figure 7. Achieved drag-reduction rate R (red) and the inner-scaled wall-normal fluctuations at the wall (green) obtained by the OC as a function of the streamwise location (x/c) within the control area on the suction side of NACA0012 and NACA4412, respectively. Note that the optimal $\overline{v_{n,w}^2}^+ = 0.25$ is indicated by dashed–dot line in magenta, and the streamwise locations where the $\overline{v_{n,w}^2}^+ > 0.25$ are indicated by dotted grey lines, respectively.

(2007) found it at $y_v^+ \approx 8.0$ in the ZPG TBL. We now examine the wall-normal position of the virtual wall as a function of x/c and the Clauser pressure-gradient parameter β (figure 8), to discuss to which extent the pressure gradient affects the location of the virtual wall. It can be observed that y_v/δ_{99} as a function of x/c decreases with the downstream development, and it drops more rapidly under milder APG conditions. On the other hand, the evolutions of y_v^+ are more complex due to the variation of the friction velocity. In particular, case OC1 exhibits a decrease first and an increase later, while the y_v^+ of cases OC2 tends to decrease, albeit with strong oscillations. With respect to β, the profiles of inner- and outer-scaled y_v of case OC2 essentially align with its evolution as a function of x/c. However, the profiles of cases OC1 reveal that the transient of y_v are clustered in an area where $\beta \approx 0.5$, corresponding to a plateau of the streamwise evolution of β (see figure 2*a*). These results suggest that the accumulative effect of the pressure gradient (i.e flow history) has an effect on the formation of the virtual-wall planes as the TBL develops.

Uniform blowing intensifies wall-normal velocity fluctuations similarly to stronger APG, with both inner- and outer-scaled profiles showing increased and more prominent outer peaks, indicating enhanced wall-normal convection. On the other hand, body-force damping intensifies the outer peak of $\overline{v_n^2}^+$ due to reduced friction velocity. The outer-scaled profiles result in significantly attenuated outer peaks and reduced values at any wall-normal distance from the viscous sublayer. The effects of control schemes on the other Reynolds stresses $\overline{uv}$ and $\overline{w^2}$ (not shown here) are similar to those on the wall-normal velocity fluctuations. Note that OC does not produce a local minimum of $\overline{w^2}$ at the virtual wall plane.

4.3. *Anisotropy invariant maps*

We now examine the AIMs for the profiles at $x/c = 0.75$ to describe how turbulent structures in the near-wall region are modified by APG and control strategies (figure 9).

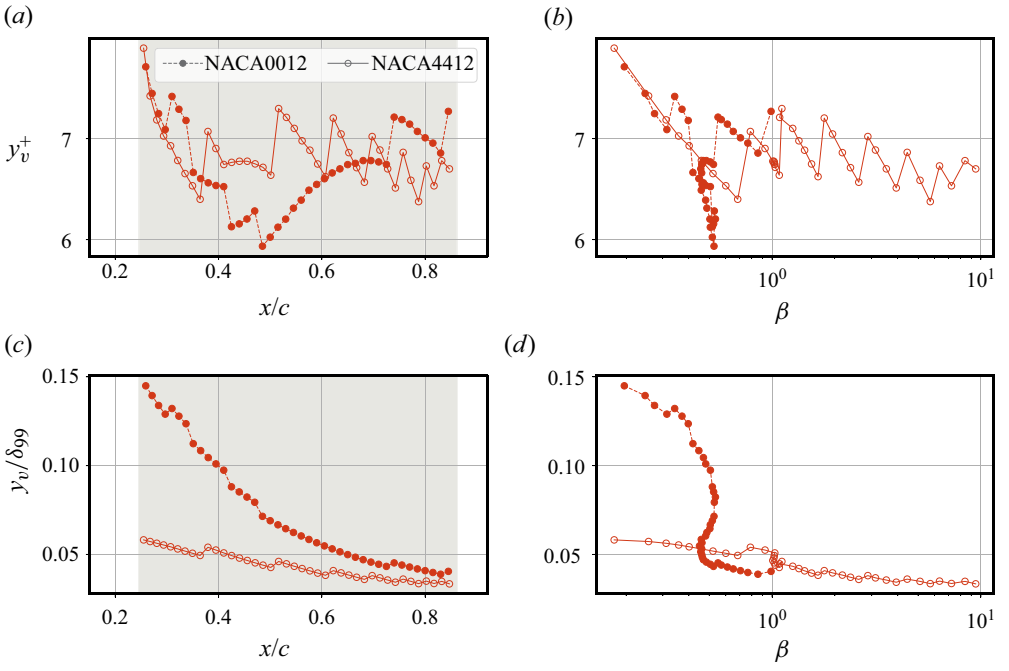

Figure 8. (*a,b*) Inner- and (*c,d*) outer-scaled wall-normal position of the virtual wall as a function of (*a,c*) the streamwise location (x/c) and (*b,d*) Clauser pressure-gradient parameter (β) in the control area (grey) on the suction side of NACA0012 and NACA4412, respectively.

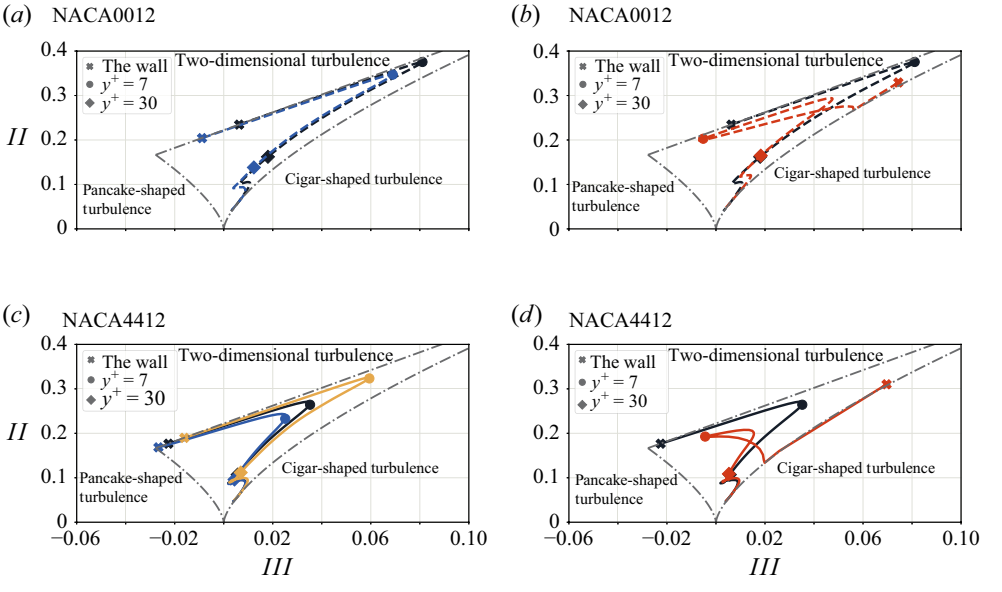

Figure 9. The second (II) and third (III) invariants of AIMs for the profiles at $x/c = 0.75$ on the suction side of (*a,b*) NACA0012 and (*c,d*) NACA4412. The limitations of the invariants are indicated by grey dashed–dot lines, and three wall-normal positions are annotated by the markers, respectively. The colour code follows table 1.

The anisotropy tensor, as introduced by Lumley & Newman (1977), is defined as

$$a_{ij} = \frac{1}{2}\frac{\overline{u_i u_j}}{k} - \frac{1}{3}\delta_{ij}\,, \tag{4.1}$$

and the AIMs are created using its second and third invariants, i.e. $II = a_{ij}a_{ji}$ and $III = a_{ij}a_{in}a_{jn}$. These plots highlight the footprint of coherent structures on the Reynolds-stress tensor, allowing to identify the various regimes at different wall-normal distances.

The uncontrolled case of NACA0012 (figure 2*a,b*) exhibits a similar pattern to that of channel flows and ZPG TBLs, while a clearer departure from canonical cases is apparent for the NACA4412 (figure 2*c,d*), where the strong APG causes a migration of the point corresponding to $y_n^+ \approx 7$ from the streak limit towards the pancake-shaped limit. This modification describes an intermediate point in the disruption of the canonical near-wall cycle in a TBL subjected to progressively stronger APGs that could eventually lead to separation, with streaks becoming progressively less important in the near-wall region.

The three control cases exhibit a remarkable variety of effects on the AIMs, despite the relatively similar skin-friction reduction. Among them, OC causes the most dramatic modifications to the AIMs. At the wall, fluctuations are introduced by the control but solely in the wall-normal direction, causing the state at that location to coincide with the cigar-shaped limit. From there, the state of the flow moves towards the two-dimensional limit until reaching the position of the virtual-wall plane ($y_n^+ \approx 7$) and then undergoes, between the virtual origin and the upper limit of the buffer region, the same evolution that in the reference cases starts at the wall. This is linked to the findings by Hammond *et al.* (1998) that the wall-normal convection does not occur below the virtual-wall plane, which was revealed by assessing the turbulent kinetic energy budgets. Besides the presence of the virtual wall, it is also apparent that streaks are less prominent in the near-wall region due to the mitigated sweep and ejection events by OC.

On the other hand, uniform blowing, examined under this specific perspective, is virtually indistinguishable from an even stronger APG. To the contrary, body-force damping causes the opposite modification in the near-wall region, making streaks more prevalent than in the uncontrolled NACA4412 case. Since uniform blowing does not introduce fluctuations and body-force damping acts in the bulk of the domain, these two strategies do not significantly alter the structure of turbulence at the wall.

5. Spectral analysis

So far, the assessment of the control mechanisms indicates that APG and OC have opposite impacts on the wall-normal momentum transport, with the APG intensifying it while OC is designed to mitigate it. Therefore, it is of great interest to investigate this interaction in terms of the energy distribution across the scales via spectral analysis.

In the present study, time series of the velocity components were obtained for a number of wall-normal profiles, spanning a total of 10 flow-over times with a sampling rate of 10^{-3} and 7.5×10^{-4} flow-over times for the NACA0012 and NACA4412 cases, respectively. We focus on the $x/c = 0.75$, and report the one- and two-dimensional power spectral densities (PSDs), which are computed using the fast Fourier transform.

Figure 10(*a*) depict the contours of the inner-scaled premultiplied PSD of wall-tangential velocity fluctuations ($k_z\phi^+_{u_t u_t}$) at $x/c = 0.75$, expressed as a function of spanwise wavelength λz and wall-normal distance y_n in inner units. Under stronger APGs, higher small-scale energy is produced in the near-wall region, and also more large-scale energy is observed in the outer region, leading to a more prominent spectral outer peak (Tanarro *et al.* 2020).

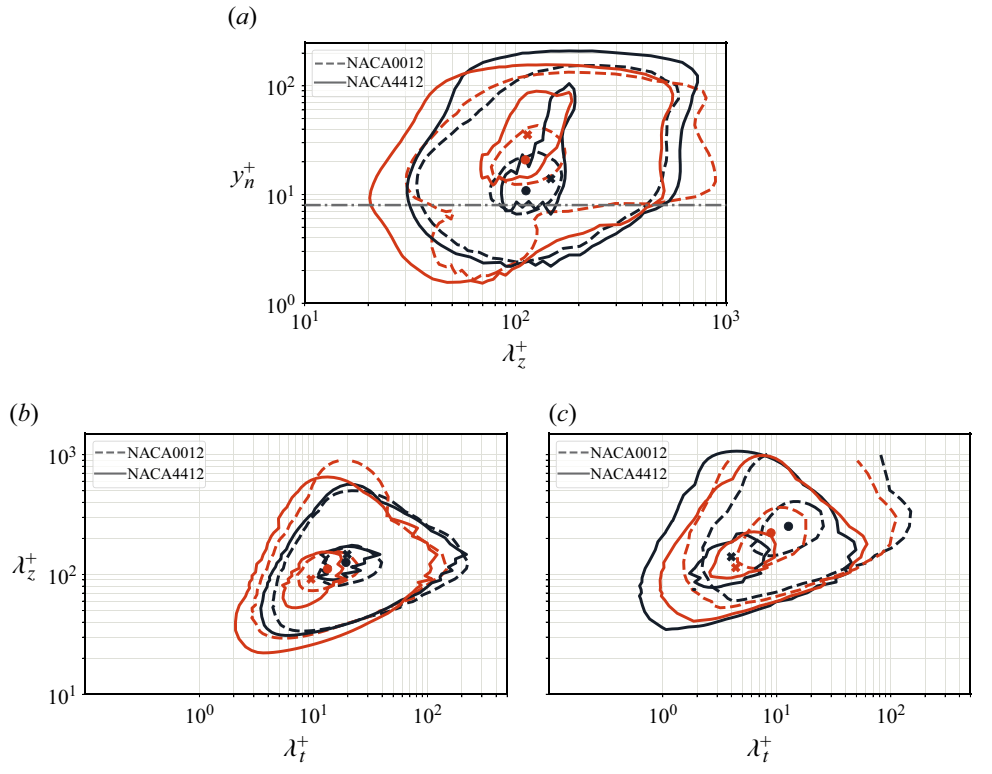

Figure 10. (*a*) Inner-scaled premultiplied spanwise PSD of the wall-tangential velocity fluctuation, in terms of the inner-scaled spanwise wavelength (λ_z^+) and wall-normal distance (y_n^+), where the position of the virtual wall plane is indicated by the dashed–dot line in grey. (*b,c)* Inner-scaled premultiplied spanwise and temporal PSD of the wall-tangential velocity fluctuations at (*b*) $y_n^+ = 15$ and (*c*) $y_n^+ = 150$. Results shown at $x/c = 0.75$ on the suction side of the NACA0012 (dashed lines) and NACA4412 (solid lines) cases. The contours illustrate the levels corresponding to 15 % and 75 % of the maximum power density in the inner region for each case, and the locations of the maxima achieved on the NACA0012 and NACA4412 are marked with circles and crosses, respectively. The colour code follows table 1.

The OC significantly alters both the value and location of the spectral inner peak. In particular, case Ref1 exhibits a magnitude of the inner peak of 4.68, whereas case OC1 results in a lower inner peak of 4.22, located at a higher wall-normal distance and slightly lower inner-scaled wavelength λ_z^+. Note that there is no outer peak for case Ref1 due to the lower pressure gradient. In contrast, case Ref2 exhibits inner and outer peaks of 5.89 and 4.82, respectively, while case OC2 enhances these values to 5.93 and 5.37, which are located farther from the wall and at lower λ_z^+. Additionally, OC attenuates energy in the outer region for any inner-scaled wavelength.

In the near-wall region, the effects of OC on the PSD vary significantly with the APG. For case OC1, below the virtual wall, only small-scale energy (ranging from $50 \leq \lambda_z^+ \leq 100$) is present, indicating that OC effectively suppresses wall-normal transport of streamwise velocity fluctuations under mild APG, but further mitigation of small-scale structures remains challenging. Above the virtual wall, case OC1 significantly energizes the large scales in the near-wall region and also energizes small scales, although less intensely. On the other hand, case OC2 exhibits a wider range of scales below the virtual wall, with less pronounced large-scale energy but further energized small scales. Above

the virtual wall, case OC2 further energizes small-scale structures below $\lambda_z^+ < 30$ without significantly modifying energy for scales larger than $\lambda_z^+ \approx 400$ in the near-wall region.

Figures 10(b) and 10(c) depict the contours of the two-dimensional spectral densities of the streamwise velocity fluctuations for OC and uncontrolled cases on the suction side at $x/c = 0.75$ and at two wall-normal distances: $y_n^+ = 15$ and $y_n^+ = 150$, respectively. Note that we employ Welch's overlapping window method for computing the PSD due to the lack of periodicity in the temporal data. At $y_n^+ = 15$, the intensified APG modifies both the intensities and shapes of the two-dimensional spectra. In particular, case Ref2 results in higher spectral density values of approximately 2.6 compared with 2.0 for case Ref1. Additionally, λ_t^+ of Ref2 is reduced, and the smallest and largest structures are expanded towards both shorter and longer wavelengths, respectively. OC reduces the PSD values to approximately 1.8 and 2.1 for cases OC1 and OC2, respectively, while the spectra are located at lower λ_z^+ and λ_t^+. Note that case OC1 further energizes large-scale structures towards longer wavelengths and periods. At $y_n^+ = 150$, the stronger APG leads to an extension of the lower-energy contour towards smaller wavelengths and shorter periods. OC again reduces the PSD values, but its effects on the contour shape vary under different pressure gradients. In particular, case OC1 increases the smallest structures, showcasing a similar effect to a stronger APG , while the energy contained within the case OC2 exhibits the opposite effect.

6. Summary and conclusions

In the current study, we analysed the effects of OC applied to the spatially developing TBL over the suction side of the NACA0012 wing section at 0° angle of attack and the NACA4412 wing section at 5° angle of attack, both at $Re_c = 200\,000$. The objective was to understand how this control scheme interacts with mild and strong APGs, respectively. Additionally, uniform blowing was considered on both wing sections, and a database where body-force damping is applied on the NACA4412 wing section (Atzori *et al.* 2021) was used for comparison between different active-flow-control schemes aimed at reducing friction drag. Overall, the performance of OC is significantly influenced by the APG: As the scheme solely depends on the off-wall observations to mitigate near-wall fluctuations, the intensified wall-normal convection due to the pressure gradient remarkably modifies the interactions between OC and TBL.

We first assessed the streamwise development of the various integral quantities. Opposition control reduces both boundary-layer thickness and friction, leading to higher β and H as well as lower Re_θ, which are more pronounced for the TBL subjected to milder pressure gradient.

Next, we evaluated the control efficiency. The achieved friction-drag reduction (R) significantly varies with the intensity of the pressure gradient: as the pressure gradient gets more intense, the achieved R gets smaller. And OC achieves maxima of $R \approx 40\,\%$ and $\approx 30\,\%$ on the NACA0012 and NACA4412, respectively, regardless of the spikes at the edge of the control section due to the change of wall boundary condition. Moreover, the assessment of energy gain (G), which involves the wall-pressure fluctuations, further reveals that applying OC on TBLs with strong-APG conditions requires dramatically higher energy input, approximately an order of magnitude higher than in mild-APG conditions. Regarding the aerodynamic effects, as the OC gets a lower drag coefficient C_d by reducing both $C_{d,f}$ and $C_{d,p}$, also leading to a slightly higher C_l, it leads to an improved aerodynamic efficiency (L/D). Specifically, OC reduces C_d by 6.8 % and 5.1 % compared with the reference C_d of NACA0012 and NACA4412, respectively.

The effects of OC were further investigated by analysing the inner- and outer-scaled wall-normal turbulence statistics at $x/c = 0.75$. First, we assess the mean wall-tangential velocity U_t, where the stronger APG energizes the wake, resulting in higher U_t in the outer region. The manipulated inner-scaled mean wall-tangential velocity results in a more prominent outer region, while in the viscous sublayer, the controlled profiles of U_t are vertically shifted downwards with respect to the reference. Subsequently, we assess the fluctuations of wall-tangential velocity components $\overline{u_t^2}$, the inner-scaled profiles of OC result in intensified inner peaks, which are slightly shifted outwards for streamwise velocity fluctuations and inwards for the other terms. This is less pronounced when the pressure gradient intensifies. Opposition control also energizes the outer peak of inner-scaled streamwise velocity fluctuations caused by a stronger pressure gradient, which is independent of the scaling.

Furthermore, the assessment of the fluctuations of wall-normal velocity components $\overline{v_n^2}$ provides physical insights in terms of the control mechanism. First, by evaluating the streamwise evolutions of $\overline{v_n^2}^+$ at the wall yield by OC, we found that the profiles gradually exceed the maximum intensity of 0.25 that guarantees the drag reduction (Chung & Talha 2011), and that location align well with where the obtained R starts descending. This is directly linked to the increased wall-normal convection caused by APGs. Another critical insight is the presence of the so-called virtual wall (Hammond *et al.* 1998), manifested by examining the local minima of the $\overline{v_n^2}$ profiles in the viscous sublayer. At $x/c = 0.75$, the plane of the virtual wall is at a wall-normal distance of $y_n^+ \approx 7$, being roughly half of the prescribed sensing plane ($y_n^+ = 15$), which reflects the effective mitigation of wall-normal momentum transport achieved by OC. The assessment of the wall-normal position of the virtual-wall plane as a function of β suggests that the pressure gradient implicitly impacts the formulation of the virtual wall. Moreover, the AIMs analysis provides insights on the control mechanism in terms of mitigating the near-wall fluctuations and the transition of the invariants at the virtual-wall plane.

The results of spectral analysis are discussed as an extension of the previous investigation on turbulence statistics. First, we assess the one-dimensional PSDs of inner-scaled Reynolds-stress tensor terms as a function of the spanwise wavelength λ_z. In general, OC results in lower PSDs and attenuates large-scale structures below the plane of the virtual wall. However, due to the transport of small scales from the near-wall region to the outer layer induced by APG (Tanarro *et al.* 2020), the interaction between OC and APG in terms of the energization of structures significantly varies with the intensity of the pressure gradient, as reflected by examining the spectral contours with lower λ_z. Essentially, when the manipulated TBL is subjected to milder APG, OC attenuates a wider range of wavelengths in the near-wall region. The structures in the outer region are not drastically modified by OC. Subsequently, we assess the two-dimensional spectra of inner-scaled streamwise velocity fluctuations as a function of spanwise wavelength and temporal information at $y_n^+ = 15$ and 150. The results further confirm that the spectral contour of OC is significantly affected by the energization of small scales in the outer region caused by APG, which is more prominent for shorter periods.

One remaining open question is how to improve the performance of OC applied to APG TBLs. In principle, a higher drag-reduction rate might be achieved through a combined-control method that imposes fluctuations of wall-normal and spanwise velocity components at the wall, as reported by Choi *et al.* (1994) and Wang *et al.* (2016). However, the performance of OC becomes unstable when the prescribed sensing plane is too far from the wall or the control intensity overloads (Choi *et al.* 1994; Hammond *et al.* 1998;

Chung & Talha 2011), whereas the calibration of the control configuration is complicated under such complex scenario, which makes the approach to be idealized rather applicable in practice.

On the other hand, deep reinforcement learning is a novel AFC approach that is demonstrating promising performance in terms of drag reduction (Guastoni *et al.* 2023; Sonoda *et al.* 2023; Suárez *et al.* 2025) and separation control (Font *et al.* 2024; Suárez *et al.* 2024). Since it takes advantage of the efficiency of neural networks at representing complex, nonlinear functions following their universal approximator property (Vinuesa *et al.* 2022), it could be a potential solution to tackle with the aforementioned challenges encountered by OC under complex scenarios, as discussed by Guastoni *et al.* (2023).

Another important point left for future studies is exploring the control performance under a broader range of angles of attack. As our results indicate that drag reduction diminishes as the APG increases the wall-normal convection, the performance of OC will likely be more significantly reduced when the angle of attack becomes larger, where flow separation becomes more pronounced and the APG is extremely strong, being both challenging and computationally expensive.

The current study describes the interaction of OC and TBLs subjected to non-uniform APG. To the best of our knowledge, this is the first study to apply OC to turbulent wings and to conduct an in-depth analysis of its effects on such complex geometries.

Acknowledgements. The simulations were run with the computational resources provided by the Swedish National Infrastructure for Computing (SNIC). The authors thank R. Mariani for his insightful comments on this manuscript.

Funding. This work is supported by the funding provided by the Swedish e-Science Research Centre (SeRC), ERC grant no. '2021-CoG-101043998, DEEPCONTROL' to R.V. Views and opinions expressed are those of the authors only and do not necessarily reflect those of the European Union or the European Research Council. Neither the European Union nor the granting authority can be held responsible for them.

Declaration of interests. The authors report no conflict of interest.

Data availability statement. The data that support the findings of this study are openly available on GitHub-KTH-FlowAI

References

Abbas, A., Bugeda, G., Ferrer, E., Fu, S., Periaux, J., Pons-Prats, J., Valero, E. & Zheng, Y. 2017 Drag reduction via turbulent boundary layer flow control. *Sci. China Technol. Sci.* **60** (9), 1281–1290.

Albers, M., Meysonnat, P.S. & Schröder, W. 2019 Actively reduced airfoil drag by transversal surface waves. *Flow Turbul. Combust.* **102** (4), 865–886.

Anderson, J.D. 1991 Fundamentals of aerodynamics. In *McGraw-Hill Series in Aeronautical and Aerospace Engineering*. 2nd edn. pp. 1. McGraw-Hill.

Atzori, M., Vinuesa, R., Fahland, G., Stroh, A., Gatti, D., Frohnapfel, B. & Schlatter, P. 2020 Aerodynamic effects of uniform blowing and suction on a NACA4412 Airfoil. *Flow Turbul. Combust.* **105** (3), 735–759.

Atzori, M., Vinuesa, R., Stroh, A., Gatti, D., Frohnapfel, B. & Schlatter, P. 2021 Uniform blowing and suction applied to nonuniform adverse-pressure-gradient wing boundary layers. *Phys. Rev. Fluids* **6** (11), 113904.

Bewley, T.R., Moin, P. & Temam, R. 2001 Dns-based predictive control of turbulence: an optimal benchmark for feedback algorithms. *J. Fluid Mech.* **447**, 179–225.

Brunton, S.L. & Noack, B.R. 2015 Closed-loop turbulence control: progress and challenges. *Appl. Mech. Rev.* **67** (5), 050801.

Choi, H., Moin, P. & Kim, J. 1994 Active turbulence control for drag reduction in wall-bounded flows. *J. Fluid Mech.* **262**, 75–110.

Chung, Y.M. & Talha, T. 2011 Effectiveness of active flow control for turbulent skin friction drag reduction. *Phys. Fluids* **23** (2), 025102.

COLLIS, S., JOSLIN, R.D., SEIFERT, A. & THEOFILIS, V. 2004 Issues in active flow control: theory, control, simulation, and experiment. *Prog. Aerosp. Sci.* **40** (4-5), 237–289.
DACOME, G., MÖRSCH, R., KOTSONIS, M. & BAARS, W.J. 2024 Opposition flow control for reducing skin-friction drag of a turbulent boundary layer. *Phys. Rev. Fluids* **9** (6), 064602.
DE MOURA, B.B., MACHADO, M.R., DEY, S. & MUKHOPADHYAY, T. 2024 Manipulating flexural waves to enhance the broadband vibration mitigation through inducing programmed disorder on smart rainbow metamaterials. *Appl. Math. Model.* **125**, 650–671.
DONG, S., KARNIADAKIS, G.E. & CHRYSSOSTOMIDIS, C. 2014 A robust and accurate outflow boundary condition for incompressible flow simulations on severely-truncated unbounded domains. *J. Comput. Phys.* **261**, 83–105.
ETO, K., KONDO, Y., FUKAGATA, K. & TOKUGAWA, N. 2019 Assessment of friction drag reduction on a clark-y airfoil by uniform blowing. *AIAA J.* **57** (7), 2774–2782.
FAHLAND, G., ATZORI, M., FREDE, A., STROH, A., FROHNAPFEL, B. & GATTI, D. 2023 Drag Assessment for Boundary Layer Control Schemes with Mass Injection. *Flow Turbul. Combust.* **113**, 119–138.
FISCHER, P.F., LOTTES, J.W. & KERKEMEIER, S.G. 2008 Nek5000 Web page. http://nek5000.mcs.anl.gov.
FONT, B., VILA, A.-Á., FRANCISCO, R., JEAN, V., Ricardo, & LEHMKUHL, O. 2024 Active flow control of a turbulent separation bubble through deep reinforcement learning. In *Journal of Physics: Conference Series*, vol. 2753, p. 012022. IOP Publishing.
FUKAGATA, K., IWAMOTO, K. & HASEGAWA, Y. 2024 Turbulent drag reduction by streamwise traveling waves of wall-normal forcing. *Annu. Rev. Fluid Mech.* **56** (1), 69–90.
FUKAGATA, K., SUGIYAMA, K. & KASAGI, N. 2009 On the lower bound of net driving power in controlled duct flows. *Physica D: Nonlinear Phenom.* **238** (13), 1082–1086.
GE, M., TIAN, D. & YONGQIAN, L. 2016 Dynamic evolution process of turbulent channel flow after opposition control. *Fluid Dyn. Res.* **49** (1), 015505.
GUASTONI, L., RABAULT, J., SCHLATTER, P., AZIZPOUR, H. & VINUESA, R. 2023 Deep reinforcement learning for turbulent drag reduction in channel flows. *Eur. Phys. J. E* **46** (4), 27.
GAD-EL HAK, M. 1996 Modern developments in flow control. *Appl. Mech. Rev.* **49** (7), 365–379.
HAMMOND, E.P., BEWLEY, T.R. & MOIN, P. 1998 Observed mechanisms for turbulence attenuation and enhancement in opposition-controlled wall-bounded flows. *Phys. Fluids* **10** (9), 2421–2423.
HARUN, Z., MONTY, J.P., MATHIS, R. & MARUSIC, I. 2013 Pressure gradient effects on the large-scale structure of turbulent boundary layers. *J. Fluid Mech.* **715**, 477–498.
HWANG, D. 1997 A proof of concept experiment for reducing skin friction by using a micro-blowing technique. In *35th Aerospace Sciences Meeting and Exhibit*, pp. 546. Legacy CDMS.
JIMÉNEZ, J., HOYAS, S., SIMENS, M.P. & MIZUNO, Y. 2010 Turbulent boundary layers and channels at moderate Reynolds numbers. *J. Fluid Mech.* **657**, 335–360.
KAMETANI, Y., FUKAGATA, K., ÖRLÜ, R. & SCHLATTER, P. 2015 Effect of uniform blowing/suction in a turbulent boundary layer at moderate Reynolds number. *Intl J. Heat Fluid Flow* **55**, 132–142.
KING, R. 2007 *Active Flow Control*. Springer.
KING, R. 2010 *Active Flow Control II*. Springer.
KRAVCHENKO, A.G., CHOI, H. & MOIN, P. 1993 On the relation of near-wall streamwise vortices to wall skin friction in turbulent boundary layers. *Phys. Fluids A: Fluid Dyn.* **5** (12), 3307–3309.
LI, Z., DANG, X., LV, P. & DUAN, H. 2021 Blowing-only opposition control: characteristics of turbulent drag reduction and implementation by deep learning. *AIP Adv.* **11** (3), 035016.
LUMLEY, J.L. & NEWMAN, G.R. 1977 The return to isotropy of homogeneous turbulence. *J. Fluid Mech.* **82** (1), 161–178.
MADAY, Y. & PATERA, A. 1989 Spectral element methods for the incompressible Navier-Stokes equations. In *State-of-the-art surveys on computational mechanics (A90-47176 21-64)*, pp. 71–143. American Society of Mechanical Engineers (ASME).
MENTER, F.R. 1994 Two-equation eddy-viscosity turbulence models for engineering applications. *AIAA J.* **32** (8), 1598–1605.
MONTY, J.P., HARUN, Z. & MARUSIC, I. 2011 A parametric study of adverse pressure gradient turbulent boundary layers. *Intl J. Heat Fluid Flow* **32** (3), 575–585.
NEGI, P.S., VINUESA, R., HANIFI, A., SCHLATTER, P. & HENNINGSON, D.S. 2018 Unsteady aerodynamic effects in small-amplitude pitch oscillations of an airfoil. *Intl J. Heat Fluid Flow* **71**, 378–391.
NOORANI, A., VINUESA, R., BRANDT, L. & SCHLATTER, P. 2016 Aspect ratio effect on particle transport in turbulent duct flows. *Phys. Fluids* **28** (11), 115103.
ORLANDI, P. & JIMÉNEZ, J. 1994 On the generation of turbulent wall friction. *Phys. Fluids* **6** (2), 634–641.

PAMIÉS, M., GARNIER, E., MERLEN, A. & SAGAUT, P. 2007 Response of a spatially developing turbulent boundary layer to active control strategies in the framework of opposition control. *Phys. Fluids* **19** (10), 108102.

PAMIÉS, M., GARNIER, É., MERLEN, A. & SAGAUT, P. 2011 Opposition control with arrayed actuators in the near-wall region of a spatially developing turbulent boundary layer. *Intl J. Heat Fluid Flow* **32** (3), 621–630.

SCHLATTER, P. & ÖRLÜ, R. 2010 Assessment of direct numerical simulation data of turbulent boundary layers. *J. Fluid Mech.* **659**, 116–126.

SCHLATTER, P. & ÖRLÜ, R. 2012 Turbulent boundary layers at moderate Reynolds numbers: inflow length and tripping effects. *J. Fluid Mech.* **710**, 5–34.

SKAARE, P.E. & KROGSTAD, P.-Å. 1994 A turbulent equilibrium boundary layer near separation. *J. Fluid Mech.* **272**, 319–348.

SONODA, T., LIU, Z., ITOH, T. & HASEGAWA, Y. 2023 Reinforcement learning of control strategies for reducing skin friction drag in a fully developed turbulent channel flow. *J. Fluid Mech.* **960**, A30.

SPALART, P.R. & WATMUFF, J.H. 1993 Experimental and numerical study of a turbulent boundary layer with pressure gradients. *J. Fluid Mech.* **249** (−1), 337–371.

STROH, A., FROHNAPFEL, B., HASEGAWA, Y., KASAGI, N. & TROPEA, C. 2012 The influence of frequency-limited and noise-contaminated sensing on reactive turbulence control schemes. *J. Turbul.* **13**, N16.

STROH, A., FROHNAPFEL, B., SCHLATTER, P. & HASEGAWA, Y. 2015 A comparison of opposition control in turbulent boundary layer and turbulent channel flow. *Phys. Fluids* **27** (7), 075101.

STROH, A., HASEGAWA, Y., SCHLATTER, P. & FROHNAPFEL, B. 2016 Global effect of local skin friction drag reduction in spatially developing turbulent boundary layer. *J. Fluid Mech.* **805**, 303–321.

SUÁREZ, P., ÁLCANTARA ÁVILA, F., MIRÓ, A., RABAULT, J., FONT, B., LEHMKUHL, O. & VINUESA, R. 2025 Active flow control for drag reduction through multi-agent reinforcement learning on a turbulent cylinder at. *Flow Turbul. Combust.*, Accepted.

SUÁREZ, P., ÁLCANTARA ÁVILA, F., RABAULT, J., MIRÓ, A., FONT, B., LEHMKUHL, O. & VINUESA, R., 2024 Flow control of three-dimensional cylinders transitioning to turbulence via multi-agent reinforcement learning. *Comms. Eng.*, Accepted.

TANARRO, Á., VINUESA, R. & SCHLATTER, P. 2020 Effect of adverse pressure gradients on turbulent wing boundary layers. *J. Fluid Mech.* **883**, A8.

VINUESA, R., BOBKE, A., ÖRLÜ, R. & SCHLATTER, P. 2016a On determining characteristic length scales in pressure-gradient turbulent boundary layers. *Phys. Fluids* **28** (5), 055101.

VINUESA, R., HOSSEINI, S.M., HANIFI, A., HENNINGSON, D.S. & SCHLATTER, P. 2017 Pressure-gradient turbulent boundary layers developing around a wing section. *Flow Turbul. Combust.* **99** (3-4), 613–641.

VINUESA, R., LEHMKUHL, O., LOZANO-DURÁN, A. & RABAULT, J. 2022 Flow control in wings and discovery of novel approaches via deep reinforcement learning. *Fluids* **7** (2), 62.

VINUESA, R., NEGI, P.S., ATZORI, M., HANIFI, A., HENNINGSON, D.S. & SCHLATTER, P. 2018 Turbulent boundary layers around wing sections up to R e c = 1 000 000. *Intl J. Heat Fluid Flow* **72**, 86–99.

VINUESA, R., PRUS, C., SCHLATTER, P. & NAGIB, H.M. 2016*b* Convergence of numerical simulations of turbulent wall-bounded flows and mean cross-flow structure of rectangular ducts. *Meccanica* **51** (12), 3025–3042.

VINUESA, R. & SCHLATTER, P. 2017 Skin-friction control of the flow around a wing section through uniform blowing. In *Proceedings of European Drag Reduction and Flow Control Meeting (EDRFCM)*,

VISWANATH, P.R. 2002 Aircraft viscous drag reduction using riblets. *Prog. Aerosp. Sci.* **38** (6–7), 571–600.

WANG, F.Z., ANIMASAUN, I.L., MUHAMMAD, T. & OKOYA, S.S. 2024 Recent advancements in fluid dynamics: drag reduction, lift generation, computational fluid dynamics, turbulence modelling, and multiphase flow. *Arab. J. Sci. Engng* **49** (8), 1–13.

WANG, Y.-S., HUANG, W.-X. & XU, C.-X. 2016 Active control for drag reduction in turbulent channel flow: the opposition control schemes revisited. *Fluid Dyn. Res.* **48** (5), 055501.

XIA, Q.-J., HUANG, W.-X., XU, C.-X. & CUI, G.-X. 2015 Direct numerical simulation of spatially developing turbulent boundary layers with opposition control. *Fluid Dyn. Res.* **47** (2), 025503.

YOUSIF, M.Z., YU, L., HOYAS, S., VINUESA, R. & LIM, H. 2023 A deep-learning approach for reconstructing 3D turbulent flows from 2D observation data. *Sci. Rep-UK* **13** (1), 2529.